ELSEVIER

Contents lists available at ScienceDirect

Additive Manufacturing

journal homepage: www.elsevier.com/locate/addma





Additive manufacturing of yttrium-stabilized tetragonal zirconia: Progressive wall collapse, martensitic transformation, and energy dissipation in micro-honeycombs

Hunter A. Rauch ^a, Huachen Cui ^b, Kendall P. Knight ^a, R. Joey Griffiths ^a, Jake K. Yoder ^a, Xiaoyu Zheng ^b, Hang Z. Yu ^a, *

ARTICLE INFO

Keywords:
Stereolithography
TZP
Architectured materials
Energy dissipation
Stress-induced martensitic transformation

ABSTRACT

For zirconia-based technical ceramics, the unique advantages of micro-architecture geometries combined with the potent mechanical and functional properties have been challenging to implement owing to additive manufacturing restrictions. In this work, we present a stereolithography-based additive manufacturing approach involving slurry development for yttrium-stabilized tetragonal zirconia polycrystals (Y-TZP), followed by printing using a custom-built large-area projection micro-stereolithography system. After post-processing, i.e., polymer burnout and sintering, 98% relative density is reached in the printed Y-TZP parts. Thanks to the good manufacturing quality, the bulk-scale Y-TZP micro-honeycombs are able to display typical stretch-dominated behavior in out-of-plane compression, showing elastic loading (Stage I) and protracted brittle failure of individual walls over a significant strain (Stage II). For a Y-TZP micro-honeycomb consisting of 5×4 hexagonal cells with a wall thickness of 300 µm and a cell diameter of 1.40 mm, the energy dissipation density is measured to be 9.45 J/g, substantially higher than other ceramic honeycombs and packings reported earlier. This energy dissipation capability is mostly attributed to the progressive wall collapse seen in Stage II deformation, in which the perimeter walls are preferentially fragmented relative to the interior walls. According to finite element analysis, this phenomenon is a result of the deviation from uniaxial compression and the presence of stress gradients in the perimeter walls. We also find evidence for stress-induced martensitic transformation in the Y-TZP micro-honeycomb after compression, which may be another contributor to the observed energy dissipation capability.

1. Introduction

The recent advances in additive manufacturing have bolstered the research efforts on polymer and metal-based architectured materials focusing on the advantageous mechanical behavior associated with complex geometries and small feature sizes [1–8]. However, architectured cellular *ceramics* are yet to be extensively explored in the context of additive manufacturing, largely due to the manufacturing constraint. Such research gaps are especially notable for an important family of technical ceramics, *partially or fully stabilized zirconia*, which is renowned for a wide variety of excellent functional and structural properties, such as shape memory and superelasticity [9–14]; transformation toughening [15]; bio-compatibility [16,17]; good ionic

conductivity [18]; and good resistance to wear, erosion, and thermal shock [19]. In particular, yttrium-stabilized tetragonal zirconia polycrystal (Y-TZP) offers the highest flexural strength of all zirconia-based materials, while allowing for stress-induced martensitic transformation for toughening. In the cellular architecture form, especially stretch-dominated structures (e.g., octet-truss; honeycomb in out-of-plane loading), Y-TZP is promising for energy dissipation, lightweight structural innovation, as well as biomedical and dental applications. The architecture form also offers a path to avoiding failure upon martensitic transformation by matching the strut width to grain size, from which the mechanical constraint from triple junctions is minimized [20].

In principle, architectured zirconia can be additively manufactured

E-mail address: hangyu@vt.edu (H.Z. Yu).

^a Department of Materials Science and Engineering, Virginia Tech, Blacksburg, VA 24061, USA

b Department of Mechanical and Aerospace Engineering, University of California Los Angeles, Los Angeles, CA 90095, USA

^{*} Corresponding author.

via stereolithography [21-30], inkjet [31], and extrusion-based approaches [32,33]. In these printing approaches, zirconia particles are mixed with polymers for printing, followed by polymer burnout and subsequent sintering to remove the porosity [34]. Compared to extrusion and inkjet, stereolithography offers better resolution and scalability to print micro-architectured ceramics on the bulk scale. The print quality by stereolithography is critically dependent on the density and refractive index of the ceramic particles, which are supported by liquid resin in suspension during the layer-by-layer selective photopolymerization. Lower density helps keep the particles in suspension without adding a lot of stabilizing additives, whereas lower refractive index of the ceramic results in better curing behavior. It is thus considerably more challenging to print zirconia-based [23] (density of 5.68 g/cm³; refractive index of 2.1) than alumina-based [35] (density of 3.95 g/cm³; refractive index of 1.6) architectures. As a result, stereolithography of zirconia architectures has been comparatively less explored. Regarding the print quality of architectured zirconia, there is also a fundamental trade-off between the processability and final zirconia part density that hinges on the solid loading fraction (i.e., volume fraction of the ceramic particles). As solid loading increases, so does green density, but the viscosity of the zirconia slurry, the likelihood of flocculation, and the amount of light scattering also increase, resulting in a significant decrease of the curing depth of the slurry [36].

Because of these processing challenges, pervasive manufacturing defects like pores and cracks are difficult to prevent, and simple strategies for additive manufacturing of high-quality architectured zirconia have remained elusive. Slurry design usually requires multiple organic components to tackle these issues (e.g., diluents, dyes, monomer blends, etc.). In previous works on zirconia additive manufacturing, most mechanical testing was limited to beam bending [25,29,37] or hardness measurements [21] rather than compression loading of the architectures—which would cause premature catastrophic failure due to the existence of flaws. When tested, therefore, the 3D printed ceramic architectures often show high specific strengths but weak specific energy dissipation capacity [38–40]. The true advantages and peculiarities from the fine, complex geometries of architectured zirconia, such as bending- or stretch-dominated mechanical behavior [2,41,42], have not been adequately demonstrated.

In this work, we present a simple approach for additive manufacturing of high-quality Y-TZP. This involves development of a high solid loading Y-TZP slurry with few organic components and sufficiently low viscosity, followed by additive manufacturing of architectures using a custom-built micro-stereolithography 3D printer and post sintering. We demonstrate this approach by printing Y-TZP microhoneycombs and show that a printed centimeter-scale hexagonal Y-TZP honeycomb architecture (300 µm feature size) performs remarkably well upon compression loading thanks to the low defect density. Compression along the out-of-plane direction results in typical multiplestage deformation behavior [42] before densification: elastic deformation of the entire honeycomb followed by stepwise failure of individual cell walls, in which the perimeter walls are preferentially fractured due to the tri-axial stress state and stress gradient. We also show direct evidence of stress-induced martensitic transformation in the printed Y-TZP architecture, which has also been observed in bending experiments of 3D printed zirconia beams [29]. During loading, the density of total energy dissipation by the printed Y-TZP micro-honeycomb is measured to be $9.45\,\mathrm{J/g}$, which is considerably higher than previous works on other ceramic honeycombs [38,40,43] or superelastic zirconia granular packings [44]. This is attributed to the combined effects of gradual collapse of the architecture and martensitic transformation.

2. Experimental and simulation methods

The 3 mol%Y₂O₃-ZrO₂ powder came as spray dried granules (Y-TZP, Tosoh Corp). The granulated powder was dispersed in ethanol with 3 wt % dispersant (Variquat 42-NS, Evonik Industries) and mixed in a high

energy ball mill (Retsch Emax) using zirconia milling media at 1350 RPM for 30 min. This broke apart the aggregated granules into $\sim\!200\,\mathrm{nm}$ particles while distributing the dispersant throughout. The ethanol slurry was dried for 12 h at 80 °C to evaporate the ethanol, and the resulting dispersant-coated powder was ball milled again at the same conditions with a liquid hexanediol diacrylate monomer (HDDA, Sigma Aldrich). The photoinitiator 2,4,6-trimethylbenzoyl diphenyl phosphine oxide (TPO, Millipore Sigma) was added in solid form by manual mixing followed by rolling at $\sim\!100$ RPM for 24 h. No diluents or dyes were added to the slurry. The slurry viscosity was characterized using a cup and bob rheometer (Texas Instruments) at shear rates from $0.1\,\mathrm{s}^{-1}$ to $100\,\mathrm{s}^{-1}$.

The curability of the slurry was assessed by spreading a thick layer on a PDMS substrate and exposing identical cross-sections to a constant-power light source (power density set to $1200\,\mathrm{mJ/cm^2}$, wavelength $405\,\mathrm{nm}$) for varying times. When a slurry is exposed to UV light, its curing behavior can be quantified by the cure depth Z_C , which is affected by the addition of ceramic particles and is described by Eq. (1):

$$Z_C = D_P \ln E / E_C \tag{1}$$

where D_P is the depth of penetration; E_C is the critical energy dose; E is the actual energy dose, which is proportional to the exposure time t_{Exp} for constant exposure power. For a ceramic slurry, the depth of penetration D_P depends on the solid loading fraction V_S and the refractive index difference Δn between the monomer and ceramic [23,45] as described by Eq. (2) (the derivation of this equation is shown in the Appendix):

$$D_P = \frac{2\lambda}{3\Delta n^2 V_S \left(\left(\frac{V_S^{max}}{V_S} \right)^{1/3} - 1 \right)}$$
 (2)

Photopolymerization and 3D printing were performed using a custom-built large-area projection micro-stereolithography system (LAP μ SL) with a pixel size of 15 μ m and a layer thickness of 15 μ m [46]. The shear rate during the printing process was measured to be $\sim 6 \text{ s}^{-1}$. The exposure power of the projector was 1200 mJ/cm². After printing, the samples were gently cleaned with isopropyl alcohol to remove uncured slurry before being cured for 1 h under a UV (ultraviolet) lamp. The wavelength of light used for both printing and curing was 405 nm. Based on thermogravimetric analysis (TGA, Texas Instruments) of the cured slurry in a similar manner to Sun and Komissarenko [28,30], the printed components were heated to 100 °C at a rate of 1 °C /min, held for 30 min, heated to 200 °C at a rate of 2 °C/min, then to 400 °C at a rate of 0.4 °C/min, and then held for 60 min to remove the organics in two stages before heating at a rate of 5 °C/min to 1700 °C for sintering. The furnace was held at 1700 °C for 2 h, and then the samples were cooled at a maximum rate of 1.5 °C/min to room temperature. The heat treatments were performed in air (Lindberg/Blue M 1700). For proof-of-concept purposes, micro-honeycombs of different wall thicknesses were printed, which were on the order of hundreds of microns. The diameter of the hexagonal cells was about 1.5 mm in all cases. The relative density of the sintered honeycombs was measured with the Archimedes method.

Several honeycombs have been printed using the presented approach. To showcase the mechanical performance achievable using the slurry and process, we particularly examined a single sintered hexagonal honeycomb with 20-unit cells, arranged in a rectangular $5\times$

4 hexagonal close packing array with wall thickness $t=300~\mu\text{m}$, wall length $l=700~\mu\text{m}$, cell diameter of 1.4 mm, and height 2.55 mm. The honeycomb had a nominal cross-sectional area of 46.75 mm², and a mass of 0.290 g, and the relative density was determined to be ~ 0.4 . After a pre-test at 2 kN to verify that the sample was mechanically sound without premature failure, the honeycomb was subjected to out-of-plane compression under displacement control. For honeycomb architectures, out-of-plane loading is associated with higher collapse strengths and is

desirable for lightweight structural applications, as seen in sandwich panels that are widely used in skis, aircraft, and space vehicles [47,48]. The load frame had a 50 kN load cell (Instron 5960), and the displacement was controlled at a rate of 0.02 mm/min. The axis of loading ran parallel with the cell walls. The test was in situ monitored from the side with a digital microscope camera (Dino-Light).

Microstructure characterization of the green and sintered bodies was performed using scanning electron microscopy (SEM, FEI Helios 600 Nanolab) after sputtering the sample surface with 7 nm of Pt/Pd. The crystallographic phases of the sintered bodies before and after mechanical testing were verified with X-Ray diffraction (XRD, Panalytical X'Pert Pro) by mounting them in a spinning sample holder with the top surface orthogonal to the plane of the X-Ray gun and the detector. The uneven surface of the samples, especially after testing, can result in minor peak shifts that restrict this phase analysis largely to qualitative assessments.

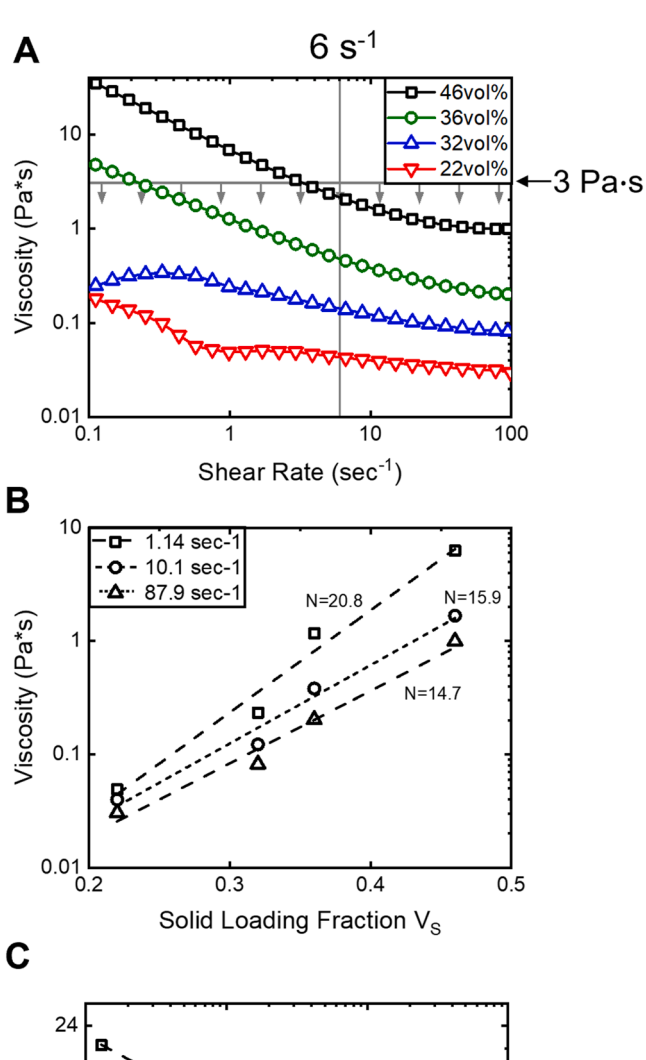
Mechanics simulation using the finite element method was performed under the same conditions as the mechanical test, at a series of axial loads up to 20 kN. The hexagonal honeycomb model with 20 cells was constructed as a solid body with 125,547 tetrahedral elements. The minimum Jacobian was 1.00, and each solid element was integrated as a selectively reduced tetrahedron with nodal rotations (ELFORM = 4). The boundary conditions were set to mimic the mechanical test, so the top and bottom surfaces were held in-plane by a fixed support condition, which disallowed translation or rotation of the topmost plane of nodes (filling the role of contact friction between the platens and sample). A boundary load was applied to the top surface. The material was assumed to be an isotropic, linear elastic solid with Young's modulus of 207 GPa and Poisson's ratio of 0.31 to match the properties of Y-TZP as reported by several suppliers [49,50]. The simulations were solved on the Virginia Tech Advanced Research Computing NewRiver cluster with LS-DYNA using nonlinear implicit time integration.

3. Y-TZP slurry development

3.1. Measurement of slurry viscosity

There is a fundamental tradeoff between green density and printability in ceramic stereolithography. If the solid loading fraction is too low, the printed parts will have low green density and will be unlikely to avoid significant warpage when firing to high density. If the solid loading fraction is too high, however, the slurry will be too viscous to flow properly. The threshold viscosity is defined as 3 Pa·s at the shear rate of our printing process, $6 \, \text{s}^{-1}$ [51]. It is optimal, therefore, to create a ceramic slurry with the highest allowable solid loading fraction that does not negatively impact the printing process. In Fig. 1(A), we plot the measured viscosity of the synthesized Y-TZP/HDDA slurry as a function of both shear rate and solid loading fraction, including 22, 32, 36, and 46 vol% Y-TZP. Generally, as the solid loading fraction increases, so does the viscosity at all shear rates; however, as the shear rate increases, the viscosity decreases, demonstrating the classical shear-thinning behavior. For this study, even with the highest solid loading fraction, i.e., 46 vol% Y-TZP powder mixed with 54 vol% HDDA, the slurry exhibits sufficiently low viscosity, which is $< 3 \text{ Pa} \cdot \text{s}$ at 6 s^{-1} . This mirrors the results from Borlaf et al. [27,52], who also found \sim 45 vol% to be the highest achievable solid loading fraction, and Komissarenko et al. [30], who showed the similar shear thinning behavior of the slurries. The 46 vol% Y-TZP slurry is thus used for printing in the rest of this manuscript.

By re-plotting the viscosity as a function of solid loading fraction V_S (Fig. 1(B)), we find that a power law of $\eta = aV_s^N$ well describes the viscosity η of all the slurries at each shear rate, where a and N are constants. As shown in Fig. 1(C), the exponent N is strongly dependent on the shear rate, suggesting that the solid loading fraction V_S has less impact on viscosity at high shear rates; the shear rate can dominate the viscosity of a highly loaded ceramic slurry that would appear quite



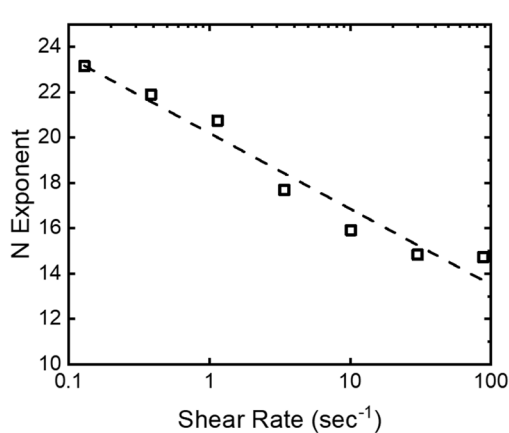


Fig. 1. Slurry viscosity control. (A) Measured viscosity of the synthesized slurry as a function of shear rate for increasing solid loading fraction, with the target viscosity highlighted. (B) Measured viscosity as a function of solid loading fraction at increasing shear rates. The results are fit with a power law with exponent N. (C) Plot of N as a function of shear rate. At higher shear rates, solid loading fraction has a reduced effect on the slurry's viscosity.

viscous under normal inspection.

3.2. Curing behavior and printability

Based on Eq. (2), we plot the theoretical prediction of penetration depth D_P as a function of V_S in Fig. 2(A). The plot indicates that the penetration depth D_P should decrease rapidly as V_S initially increases because of the light-ceramic particle interaction but will increase rapidly as V_S approaches $V_S^{max} = 0.6$ due to the significant reduction of

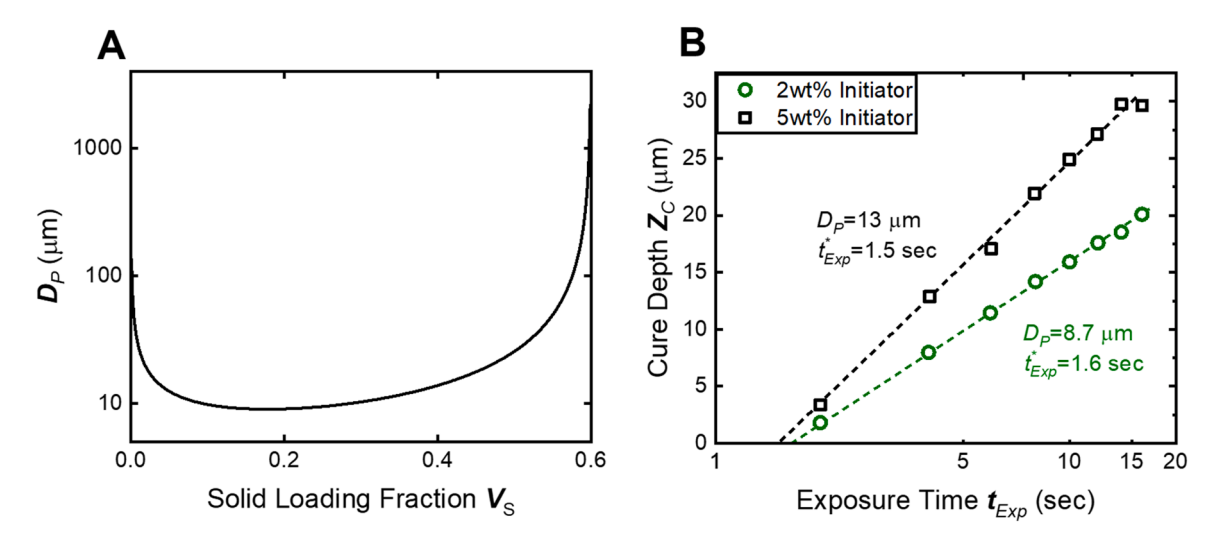


Fig. 2. Printability. (A) Theoretical prediction of D_P as a function of solid loading fraction, assuming zirconia powder and HDDA monomer following Eq. (2). (B) Measured working curves: semi-log plot of cure depth as a function of exposure time for two photoinitiator concentrations. D_P and t^*_{Exp} values are extracted from fitting with Eq. (1).

interparticle spacing.

After theoretical prediction, we experimentally examine the curing behavior and printability of the synthesized 46 vol% Y-TZP slurry, for which two different TPO photoinitiator concentrations are investigated, 2 wt% and 5 wt% relative to the HDDA concentration. For these two scenarios, Eq. (2) gives the predicted D_P value to be 17.1 and 16.5 μ m, respectively. We measure the cure depth at a series of exposure times under constant irradiation power and construct the working curves for these two cases in Fig. 2(B). By fitting the measured working curves using Eq. (1), the values of penetration depth D_P and *critical* exposure time t_{Exp}^* (corresponding to the critical energy dose E_C) are extracted. For the 2 wt% addition of TPO initiators, D_P is experimentally determined to

be 8.7 μ m, lower than the theoretically predicted value of 17.1 μ m by a substantial margin. This is possibly caused by insufficient conversion of monomers upon irradiation. When the initiator concentration is raised to 5 wt%, the measured D_P value is 13.0 μ m, which is closer to the calculated value 16.5 μ m, suggesting that the photopolymerization reaction is more complete.

Small TPO additions (i.e., 1–5%) are usually sufficient for curability [53], but the remaining discrepancy between the calculated and observed D_P values could be a sign that the solid TPO is not perfectly dissolved in the HDDA [54]. Nevertheless, based on these curability test results, we have decided to employ the Y-TZP slurry with 5 wt% TPO initiators for printing, for which the critical exposure time t_{EXP}^* is 1.5 s at

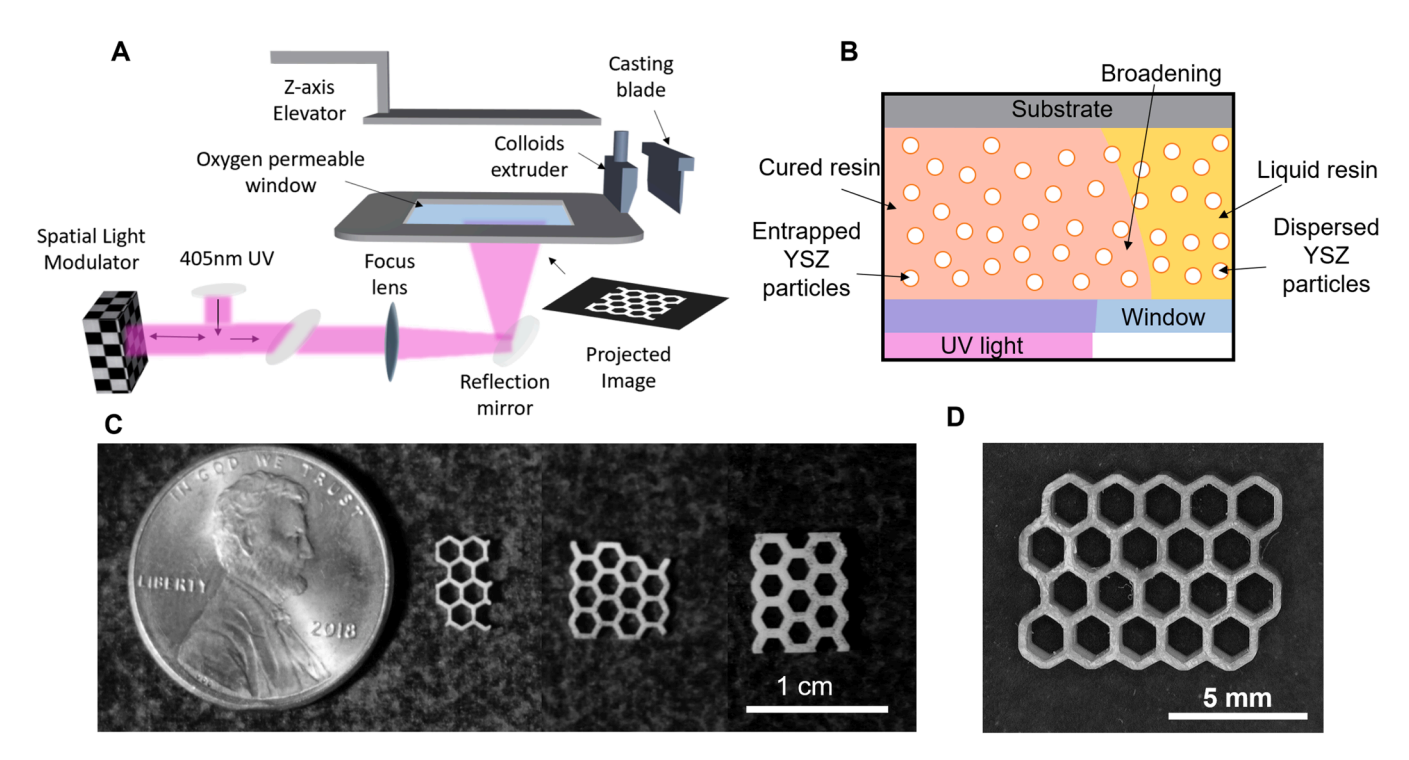


Fig. 3. Stereolithography of Y-TZP micro-honeycombs. (A) Diagram of the LAPuSL printer. A colloid extrusion head and casting blade control the layer height and ensure even spreading of the Y-TZP resin. The light source is projected digitally to pattern an image with high resolution (15 μm pixel size) onto a single layer of resin at a time. (B) Schematic of printing process during exposure of a single layer, side view. UV light enters the resin layer from the bottom and cures the resin, trapping the particles inside. During curing, the particles scatter the photons and broaden the cured volume. (C). Examples of several printed and sintered honeycomb structures with irregular macroscopic geometries. (D) A printed and sintered Y-TZP micro-honeycomb with a rectangular 5 × 4 hexagonal close packing array.

a power of 1200 mJ/cm^2 . To achieve high spatial resolution, we use the minimum step size of $15 \, \mu \text{m}$ for layer thickness and set the exposure time to be $15 \, \text{s}$ ($t_{Exp}/t_{Exp}^* = 10$), which leads to a cure depth \mathbf{Z}_C of $30 \, \mu \text{m}$ and an in-plane cure breadth of $\sim 30 \, \mu \text{m}$. This promotes inter-laminar adhesion as \mathbf{Z}_C is twice of the layer thickness [46].

4. Stereolithography of Y-TZP micro-honeycombs

The custom-built LAP μ SL system diagrammed in Fig. 3(A) is used to print Y-TZP micro-honeycombs layer-by-layer. The printing of each layer starts with a spreading process, wherein the extruder nozzle and casting blade create a thin, uniform coating of fluid resin on the window. This spreading process has a relatively high shear rate ($\sim 6~s^{-1}$) compared to vat-based stereolithography, which interacts favorably with the resin to enable even spreading [55]. As determined in the previous section, to print the synthesized Y-TZP resin in this work, the optimal print layer thickness is set at 15 μ m and the exposure time is set at 15 s.

For printing, the substrate is lowered into position, leaving a 15 μm thick layer of resin between it and the window. The UV light is then projected through the window in the desired cross-sectional pattern for 15 s, curing the exposed regions of the resin as diagrammed in Fig. 3(B) and trapping the suspended Y-TZP particles inside the now solid polymer. After exposure, the substrate – with printed material attached – is lifted to allow the casting blade to clean the uncured resin off the window, and the extruder head then spreads the next layer. This process continues until the desired part is printed.

Fig. 3(C) shows several examples of the printed honeycombs with similar cell diameters (ranging from 1.3 mm to 1.5 mm after sintering), but different wall thicknesses, which are 270 μm , 370 μm , and 640 μm from the left to the right. These samples are for proof-of-concept purposes and are not tested for mechanical performance. Such trial runs aid in determining the optimal printing and sintering parameters, based on which a Y-TZP micro-honeycomb consisting of a rectangular 5×4 hexagonal cell array is printed with the sintered wall thickness being 300 μm and cell diameter being 1.40 ± 0.08 mm (Fig. 3(D)). This Y-TZP micro-honeycomb is investigated in detail for printing quality and

mechanical behavior in the rest of this manuscript.

We characterize the printed specimens at each processing step and begin our analysis with the green bodies (Fig. 4). After printing and manual cleaning with isopropyl alcohol to remove uncured slurry, the green bodies are characterized by good dimensional accuracy and surface finish (Fig. 4(B)). Some contamination is present in the green bodies, visible extending from the printed walls into the empty space, but this is mostly dust trapped between layers. Examining the green body from the side in Fig. 4(C), individual layers are discernable due to the broadening effect during printing. This presents a small rippling effect, with a peak-to-trough height of roughly 5 μm . A closer examination of the interface between two layers with backscatter electron imaging (Fig. 4(D)) reveals a homogeneous distribution of small Y-TZP particles. If the Y-TZP slurry settled during printing, as can happen with less stable ceramic slurries [56], this region would show a particle density gradient that would result in anisotropic shrinkage during firing. The lack of such a gradient suggests that interlaminar defects are unlikely to exist in the green bodies despite the rippled outward appearance.

Next, the green bodies are debinded and sintered at 1700 °C in air, which results in ~ 20% linear shrinkage rates (measured with cuboid samples) and a final density of 98%. As seen in Fig. 5(A), and (B), the sintered specimen shows good surface quality without apparent defects. Fig. 5(C) shows a micrograph of the side of the sintered honeycomb, where the different layers are more visible than those in the green body due to coarsening during firing. The uneven, layer-by-layer patterns on the lateral side may become local stress risers and cause pre-mature failure when the honeycomb is subjected to mechanical loading. Each layer is reduced in thickness to \sim 12 μ m, with equiaxed grains making up the surface. Fig. 5(D) highlights the microstructure with a view of the unpolished top of the honeycomb, which is quite flat and looks typical for zirconia ceramics. The grain size in the sintered honeycomb is \sim 1-3 µm, much greater than the \sim 200 nm particle size in the green bodies. This is expected with the high temperature heat treatment that allows the honeycomb to achieve high density with grain growth occurring at the same time.

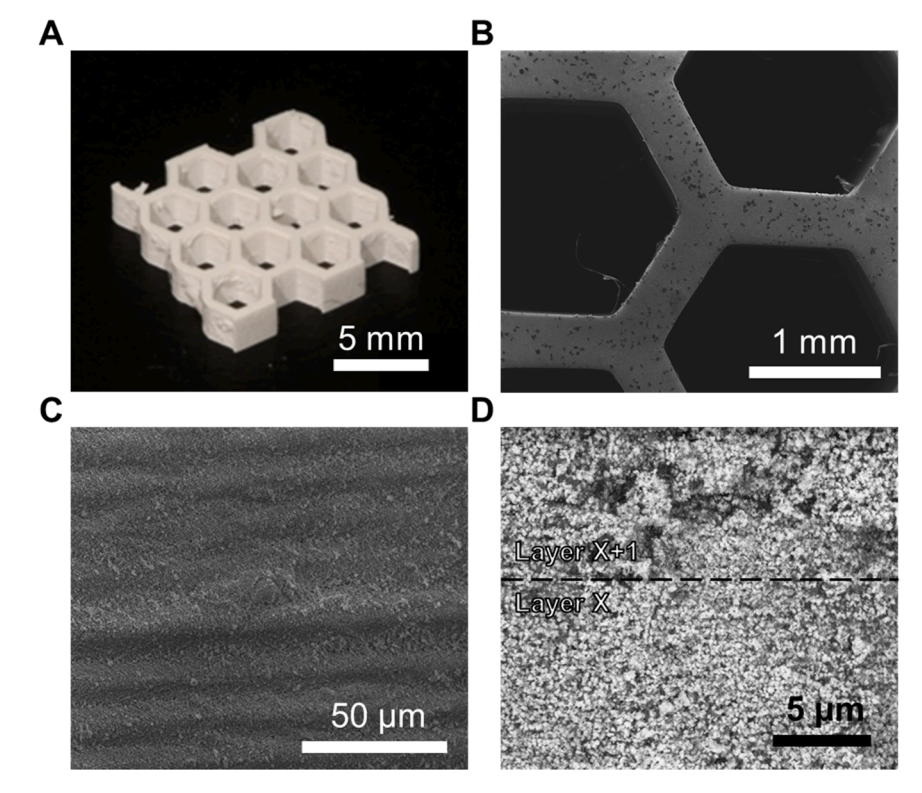


Fig. 4. 3D Printed Honeycomb Green Body. (A) Photograph of a representative as-printed honeycomb sample. (B) Secondary electron micrograph of green body from top. The dark spots are carbonaceous contamination. (C) Secondary electron micrograph of green body from side. The layer lines are visible. (D) Backscatter electron micrograph of interlaminar region. The bright spots are discrete $\rm ZrO_2$ particles. The particles are not observed to segregate, even at the top or bottom of a layer as indicated by the marked transition between Layer X and Layer X + 1.

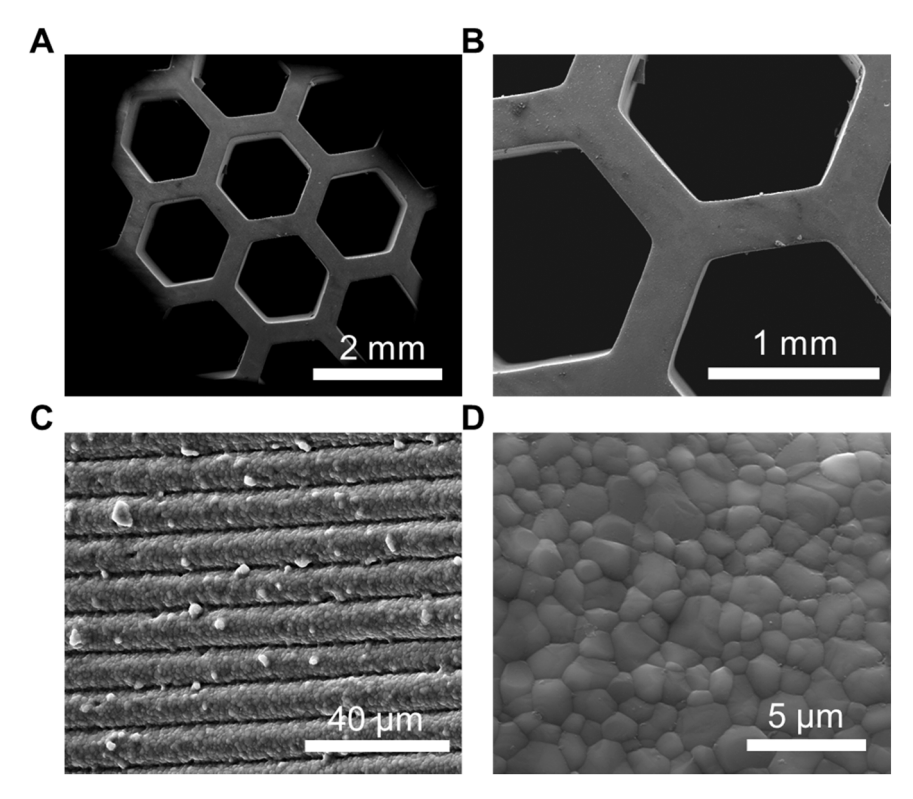


Fig. 5. Sintered Honeycomb. (A) Secondary electron micrograph from the top showing good quality after sintering. (B) Secondary electron micrograph from the top at a higher magnification. The wall thickness after sintering is ~ 0.3 mm. (C) Secondary electron micrograph of the sintered honeycomb sample from the side. The layer lines are prominent. (D) Secondary electron micrograph of the top showing an equiaxed, dense microstructure after sintering.

5. Mechanical response and phase transformation

5.1. Deformation and failure

Fig. 6(A) plots the measured homogenized stress (load divided by the nominal cross-sectional area) vs. strain curve of the selected honeycomb consisting of a rectangular 5×4 hexagonal cell array (described in

Section 2), which exhibits two-stage deformation behavior typical to cellular ceramic structures [42]. Stage I (black line) is characterized by elastic deformation of the honeycomb until a maximum stress of 268 MPa is reached, followed by a drastic decrease of the stress accompanied by structure collapse. According to the mechanics theory for cellular solids, the expected collapse stress for cellular Y-TZP with 40% relative density should be higher [42,49], but the geometry of this

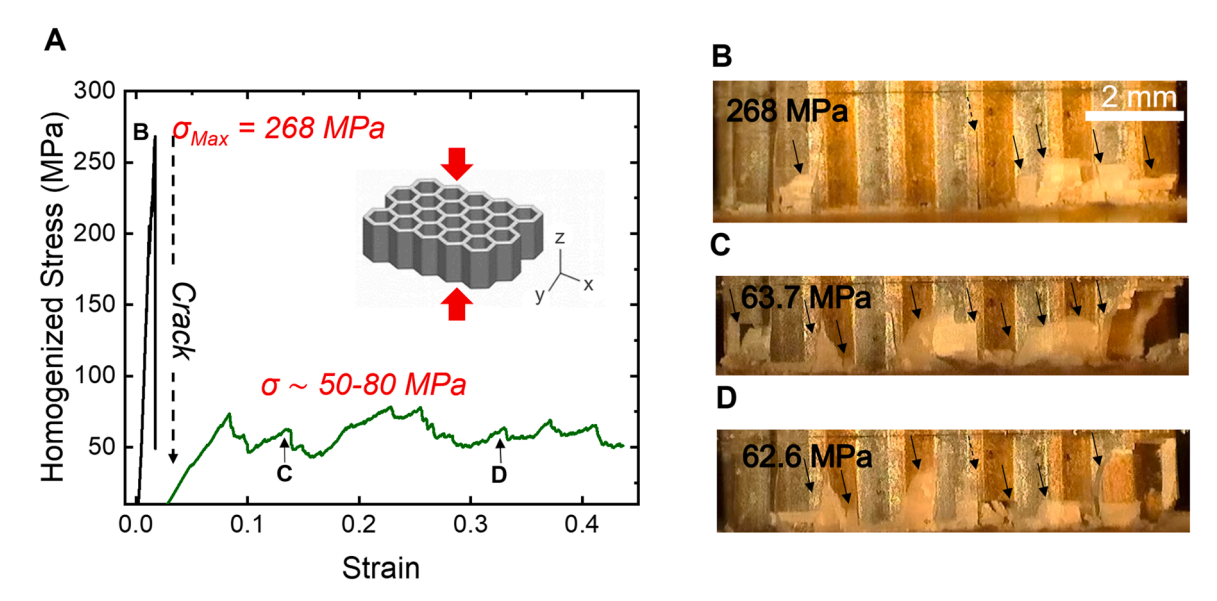


Fig. 6. Mechanical behavior of the printed Y-TZP micro-honeycomb under out-of-plane compression. (A) The measured homogenized stress vs. strain curve, showing distinct behavior for two stages. Stage I: from the initial loading to the major crack formation (black curve); Stage II: re-loading after the first failure, in which cells collapse with substantial fragmentation (green curve). Inset: illustration of the sample geometry and orientation with respect to the X-, Y-, Z-axes. (B), (C), and (D) show video snapshots corresponding to three loading steps in Stage I and Stage II labeled in (A). The snapshots are taken on the X-Z plane with black arrows indicating cracks. The periodic light and dark regions are honeycomb faces oriented towards or away from the light source, respectively.

particular sample prompts a divergence from the predicted behavior (see Section 6). The resultant failure mainly appears at the right bottom, showing fracture and fragmentation of the printed walls in Fig. 6(B). Despite the load drop associated with this local failure of the honeycomb, most of the sample is still visibly intact. This allows for reapplying the load: in Stage II (green line in Fig. 6(A)), after the initial elastic deformation, the homogenized stress is seen to oscillate around a sustained value $\sim 50\text{-}80$ MPa despite the significant increase of strain. Featuring a high collapse strength followed by a 'plateau' at considerably lower stress levels, the observed two-stage deformation (before densification) in the printed Y-TZP honeycomb is consistent with stretch-dominated structures predicted by the cellular materials literature [42]. This may be representative for the behavior by architectures made of brittle constituent materials.

There is strong correlation between the stress oscillation behavior in Stage II and local fracture events. Fig. 6(C)-(D) shows the piecemeal failure with snapshots from the test, wherein small sections of the exterior of the honeycomb, usually relegated to single wall segments, break off individually. These fracture events are each associated with small jerks observed in Fig. 6(A). The sensitivity of such correlation is further enhanced because of the small number of cells: there are only 77 walls in this sample and any fracture in one of them makes a considerable impact on the global mechanical behavior. Interestingly, even though multiple local fracture events occur in Stage II, the stress level stays in a characteristic range—some of the load drops are quite gradual in comparison to the dramatic failure that marks the end of Stage I compression. This observation indicates slow crack propagation in some cell walls in Stage II deformation.

5.2. Stress-induced martensitic transformation

After the mechanical test, a few cells on the perimeter of the honeycomb are seen to fracture and break off, becoming debris and flakes, while the majority of the honeycomb remains complete. XRD is employed to discern the crystal structure of the compressed Y-TZP micro-honeycomb and the recovered fragments, with a comparison to the as-sintered structure before compression. As shown in Fig. 7, while both cases mainly show peaks corresponding to the tetragonal phase of zirconia as expected, the post-compressed honeycomb exhibits small peaks (e.g., the $(\bar{1}11)$ and (111) peaks) that indicate the presence of ~ 10 vol% monoclinic zirconia. The stress-induced martensitic phase transformation is known to occur in yttrium-doped zirconia [57], particularly during crack propagation (as in transformation toughening [58]), and the observation in Fig. 7 shows the first direct evidence of this transformation in architectured Y-TZP. The martensitic transformation probably happens near the end of Stage I and during most of Stage II.

Stress-induced martensitic transformation in yttrium-doped zirconia is characterized by large shear strain of \sim 15% and volume change of \sim 4.5% [57]. The wall thickness of the micro-honeycomb architecture is 300 μm, whereas the grain size is measured to be 1–3 μm. Therefore, there are numerous triple junctions across the walls, imposing significant mechanical constraint for transformation among neighboring grains. With high mechanical constraint and large transformation strain, this transformation invariably generates significant internal stresses. Moreover, for the Y-TZP containing 3 mol% Y₂O₃ in this study, stress-induced martensitic transformation occurs more readily after alignment of the nanoscale ferroelastic tetragonal domains by applying sufficiently high stress [59]; without self-accommodating twins and autocatalytic transformation due to the crystallographic restrictions in this specific composition [57], the transformed volume should be localized. Given all of these considerations, the onset of stress-induced martensitic transformation is exceptionally likely to result in significant fracture events in the brittle Y-TZP micro-honeycombs [60].

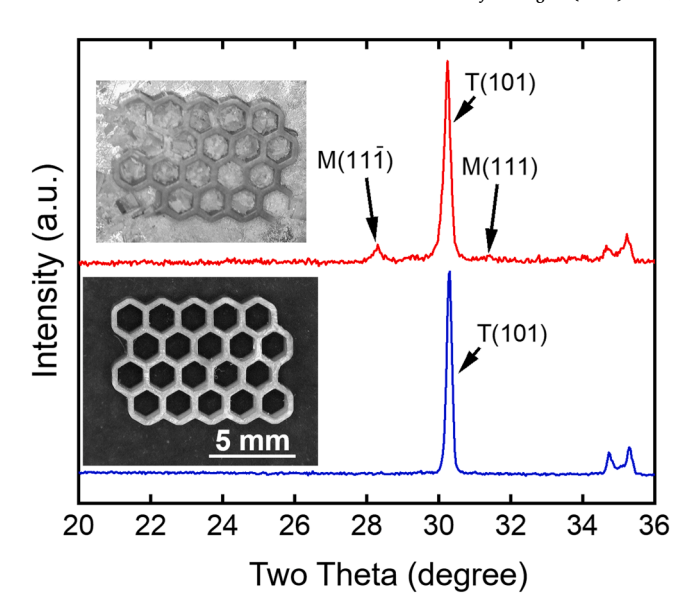


Fig. 7. Stress-Induced Phase Transformation in Y-TZP Honeycomb. The bottom XRD pattern (in blue) shows the honeycomb is in the tetragonal phase before compression, while the top XRD pattern (in red) shows the honeycomb partially transforms to the monoclinic phase after compression.

6. Mechanics analysis and discussion

6.1. Local fracture events: perimeter wall vs. interior wall

Fig. 8 (A) shows a photograph of the honeycomb after testing, which can be characterized by several types of scenarios: 1) intact surfaces that look the same as before testing, 2) damaged surfaces which have been cracked, 3) small flakes that pile up in the void space between cell walls, and 4) large fragments of the walls that break off in chunks. A closer examination of the video snapshots from in situ monitoring reveals major differences between the perimeter walls and interior walls during out-of-plane compression. From the side view, the cell walls on the perimeter of the honeycomb structure (Fig. 8(B)-(C)) appear to break off large chunks in single fracture events, with the fracture surfaces running parallel to the loading direction along the perimeter nodes and perpendicular to the loading direction across the length of the perimeter walls. The perimeter walls do not seem to fracture parallel to the loading direction through their thickness. In contrast, the cell walls on the interior of the honeycomb (Fig. 8(D)-(E)) produce small flakes of debris, with fracture apparently occurring parallel to the loading direction through the thickness of the wall. The large fracture events preferentially occur in the perimeter wall first with more significant impact on the structural integrity.

6.2. Finite element analysis

The tested Y-TZP micro-honeycomb differs significantly from the ideal cellular structure. First, the relative density is high (\sim 0.4) and the walls are thick compared to the cell diameter. Second, the cell number is small, and a significant portion of the walls are on the perimeter: there are 34 perimeter walls and 43 interior walls. Instead of directly applying the mechanics theory for cellular solids, therefore, we employ finite element analysis to understand the mechanical response of this particular Y-TZP micro-honeycomb. Out-of-plane compression of honeycomb structures leads to compression-dominated stress states in the walls, under which ceramics typically fail by shear (or a combination of shear and compression) rather than by tension, following the Coulomb-Mohr criterion [61]. More importantly, the local fracture is possibly triggered by stress-induced martensitic transformation, which corresponds to a shear-dominant shape change with the kinetics and morphology

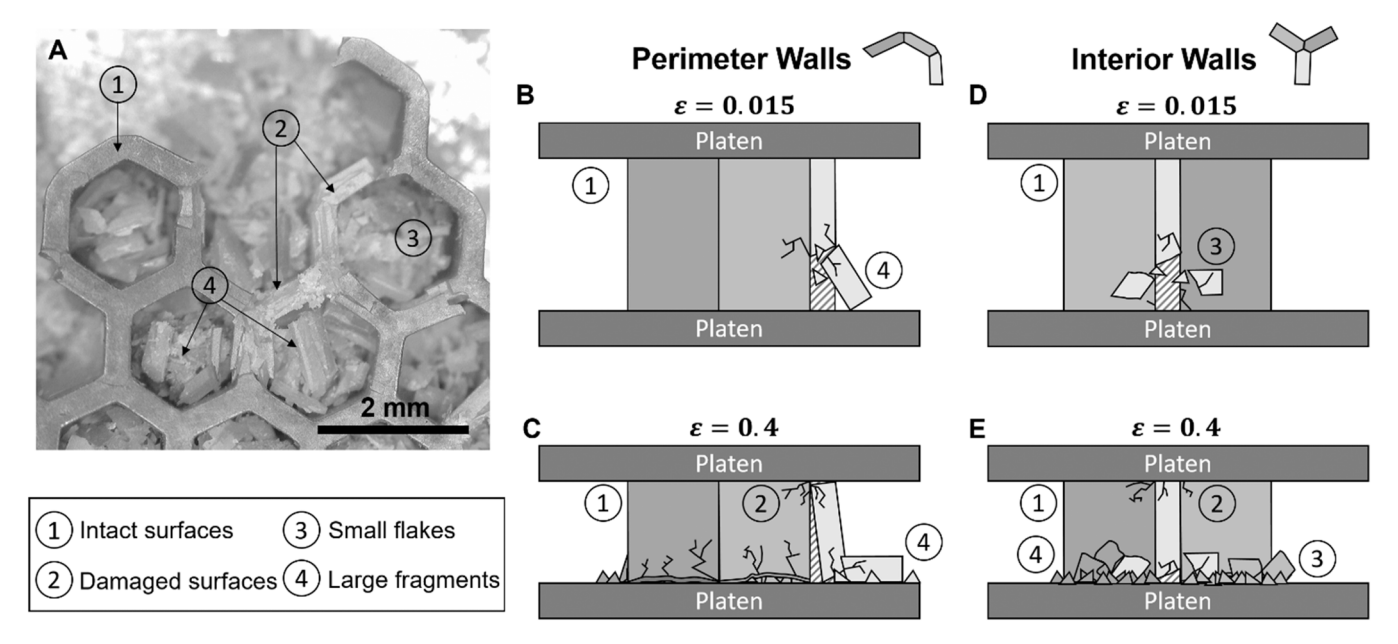


Fig. 8. Observed honeycomb failure mechanisms. (A) Photograph of the honeycomb after mechanical testing with characteristic features labeled. (B) X-Z cross sectional diagram of cell walls on the perimeter of the honeycomb at the end of Stage I compression, (C) the same cross section at the end of Stage II compression. (D) X-Z cross sectional diagram of cell walls on the interior of the honeycomb at the end of Stage I compression, (E) the same cross section near the end of Stage II compression.

determined by shear-strain energy [44]. Overall, a shear deformation criterion related to the distortion energy is proper for mechanics analysis of the target problem.

Fig. 9(A) shows the von Mises stress distribution in a cross-section of the entire honeycomb at Z = 1.275 mm (i.e., the midpoint of the walls). The applied force in Fig. 9(A) is 3600 N, which corresponds to a homogenized stress of $\sim\!77$ MPa. This simulated stress distribution corresponds to the state of the honeycomb during linear elastic deformation in Stage I compression, but there are already interesting anomalies to note. For one, there are stress gradients of 20–60 MPa present along the length l of individual walls on both the perimeter and interior of the entire structure. There are also stress concentrations on the inner faces of the perimeter walls with strong gradients of stress towards the outermost corners – as extreme as \sim 60 MPa change in von Mises stress over a distance of \sim 0.5 mm. These effects are highly localized and indicate that the mechanical performance of the honeycomb as a whole is likely to deviate from the predictions by homogenized treatment [7].

Fig. 9(B) tracks the evolution of the von Mises stress distribution in the perimeter wall circled in Fig. 9(A) over three stages of loading that correspond to homogenized stresses of 85.6, 257, and 428 MPa, respectively. Although the honeycomb never reached 428 MPa in experiment, the simulated data point is useful for extrapolation and revealing more physical insights. In each histogram, the nodallyaveraged stress distribution becomes broader and trends towards higher median stress values. The bounds of high and low values also grow as the applied load is increased. In comparison, the interior wall has much less heterogeneous stress distributions, exhibiting much tighter stress distribution histograms in Fig. 9(D) than the perimeter wall in Fig. 9 (B). The physical picture of the stress distribution in perimeter and interior walls is reflected in Fig. 9(C) and (E), which show the X-Z cross section of the two types of walls under the maximum loading in simulation. The top and bottom of the wall have been truncated and the horizontal displacement is magnified 50 times for clarity. The perimeter wall is clearly bowing outwards and has higher von Mises stress on the inner face than on the outer face, whereas the interior wall remains straight without discernable bowing or distortion. Note that under 257 MPa homogenized stress, the nodal von-Mises stress values can be as high as ~1.4 GPa (Fig. 9(B) and (D)). This sheds light on how and

where the martensitic phase transformation might be triggered with stress.

The perimeter walls are thus characterized by stress gradients as well as tri-axial stress states, bending moments, and possible stress-induced martensitic transformation, in many ways deviating from uniaxial compression. This makes them more susceptible to local fracture than the interior walls—a phenomenon observed from the in situ monitoring and illustrated in Fig. 8. This is why the perimeter walls are seen to fracture first in out-of-plane compression. As the perimeter walls fail in sequence and can no longer support load individually, the interior walls begin to act like perimeter walls and fail in a similar manner. Considering the bending moment in the perimeter wall, we may use the *flexural strength*, instead of *compressive strength*, of Y-TZP when estimating the collapse strength of the micro-honeycomb. With the relative density of 0.4 and the measured flexural strength of ~550–1000 MPa [25,62], this would predict the collapse stress ~220–400 MPa [42], which is more consistent with the observed value of 268 MPa in Fig. 6.

6.3. Energy dissipation capacity

By integration under both stages of the stress-strain curve in Fig. 6, the density of energy dissipation during mechanical testing is calculated to be $23.0~\text{MJ/m}^3$, with $\sim 90\%$ of the energy dissipated during Stage II. With the nominal cross-sectional area of $46.75~\text{mm}^2$ and height of 2.55~mm, the entire Y-TZP micro-honeycomb dissipates 2.74~J of energy. Considering the honeycomb mass of 0.290~g, the energy dissipation capacity per mass is 9.45~J/g even without reaching the densification stage of compression. In a similar set of experiments on cordierite and mullite square-walled honeycombs, Jain et al. found that out-of-plane compression leads to a total potential dissipative capacity of only $\sim 3~\text{J/g}$ by considering the full densification regime [43], substantially lower than the results in this work.

The energy dissipation capacity in this work mainly originates from the protracted, element-by-element, gradual wall collapse in Stage II. This behavior and the corresponding energy dissipation capacity have not been demonstrated previously in additively manufactured zirconia architectures because of the high defect levels, which would initiate failure at much lower stress levels. Stress-induced martensitic

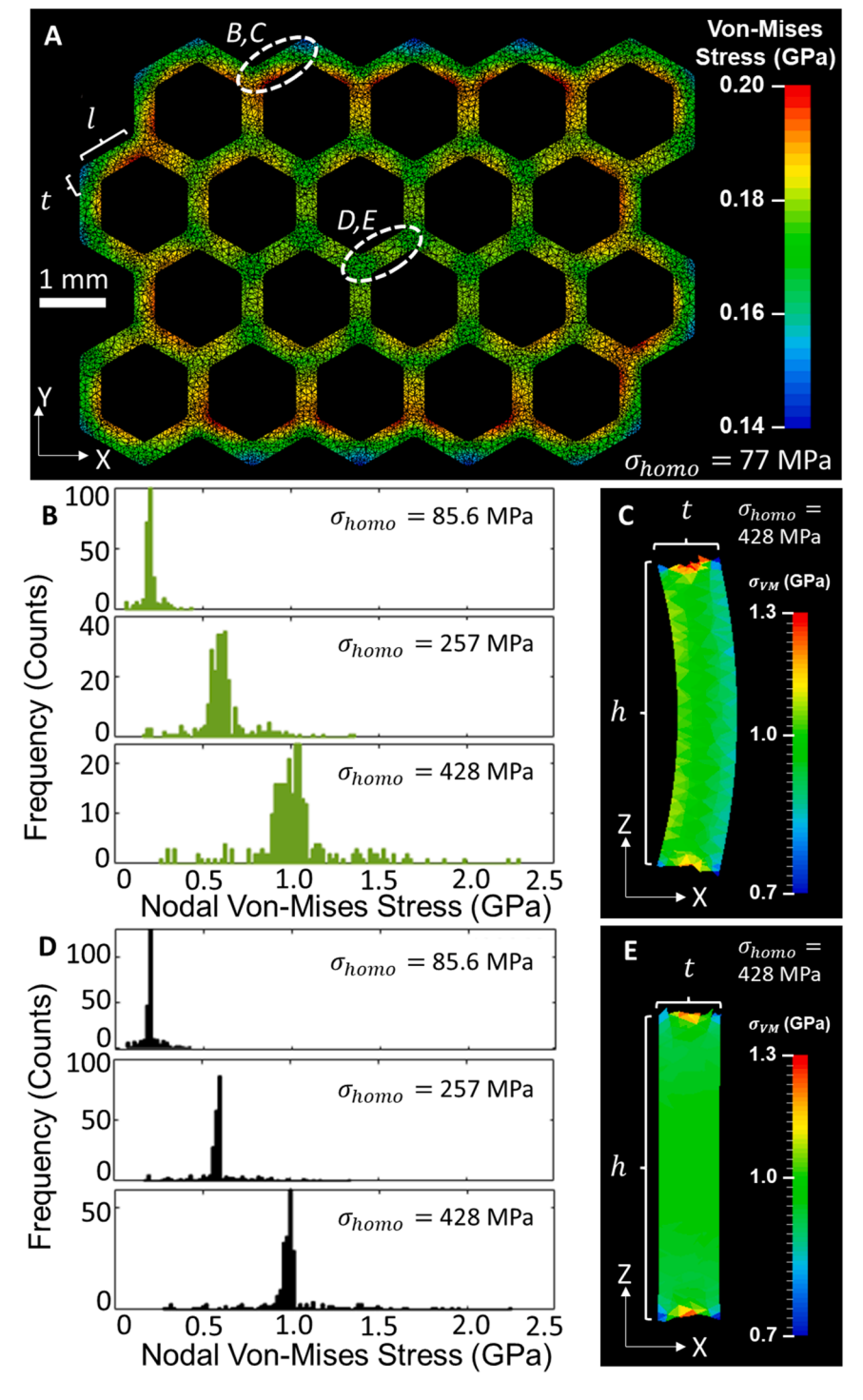


Fig. 9. Finite element analysis. (A) Von Mises stress distribution in X-Y cross-section of the simulated honeycomb at homogenized stress of 77 MPa. (B) Histograms of nodally-averaged von Mises stress in the perimeter wall indicated with dotted circle in A. (C) X-Z cross-section (orthogonal to the faces) of the perimeter wall at homogenized stress of 428 MPa, displacement values multiplied by 50x for clarity. (D) Histograms of interior wall stresses. (E) X-Z cross section of interior wall, with displacement multiplied by 50x.

transformation from the tetragonal to the monoclinic phases can also contribute to energy dissipation. Yu et al. found that the bulk energy absorption density by ceria-stabilized zirconia granular packings is $\sim 2~\mathrm{J/g}$ [44]. Du et al. found that a fully transforming single crystal particle of ceria-stabilized zirconia might dissipate $\sim 6~\mathrm{J/g}$ at maximum [63]. Fig. 7 shows that the transformation volume is only $\sim 10\%$, which would equate to $0.2{-}0.6~\mathrm{J/g}$ energy dissipation. As a result, stress-induced martensitic transformation is a minor mechanism for energy dissipation in this instance.

Although the energy dissipation level (9.45 J/g) in Y-TZP microhoneycomb is not exceptional [64] in comparison with metallic counterparts, this work serves as a testament to the mechanical performance

and energy dissipation capabilities of brittle, ceramic-based architectures. With good part quality enabled by the additive manufacturing strategy presented here, these structures have promising applications in high temperature, corrosive, irradiating, or other harsh environments where metals can suffer from accelerated damages.

7. Conclusions

A simple Y-TZP slurry has been created for stereolithography-based additive manufacturing, from which high-quality, bulk-scale Y-TZP micro-honeycombs are printed by utilizing a custom-built large-area projection micro-stereolithography system. When loaded, the sintered

Y-TZP micro-honeycombs show intriguing behavior, including progressive wall collapse, stress-induced martensitic transformation, and good energy dissipation capacity. The most important results from this work include:

- The slurry is 46 vol% Y-TZP dispersed in HDDA monomer with TPO photoinitiator and no additional diluents or dyes. A viscosity <3 Pa•s is achieved at a shear rate of 6 s $^{-1}$; a cure depth of 30 μm is achieved after 15 s of exposure at 1200 mJ/cm² with 405 nm light wavelength. Y-TZP honeycombs are printed with a 15 μm layer thickness. One honeycomb of \sim 40% relative density with 300 μm -thick walls and a 5 \times 4 hexagonal cell design is used for further testing. After burnout and sintering at 1700 °C for 2 h, this honeycomb is densified to \sim 98% of the theoretical density.
- Out-of-plane mechanical compression of the selected honeycomb shows 1) elastic loading with a maximum homogenized stress of 268 MPa, and 2) protracted brittle failure over ~ 40% strain with nominal homogenized stress ~50–80 MPa. Thanks to the good manufacturing quality, the printed Y-TZP micro-honeycomb shows good energy dissipation capacity, with the energy dissipation density measured to be 9.45 J/g.
- Finite element analysis reveals that the stresses in the perimeter cell
 walls are heterogeneous with the stress-state deviating from uniaxial
 compression. This makes them more susceptible to local fracture
 than the interior walls, which is consistent with the observation
 during loading.
- Before mechanical testing, the Y-TZP micro-honeycomb is in 100% tetragonal phase. After compression and fracture, a small amount of the monoclinic phase arises, showing direct evidence for stressinduced martensitic transformation in the printed Y-TZP microhoneycomb.

Intellectual property disclosure statement

The Virginia Tech team (Rauch, Griffiths, Yoder, Yu, Arvan, Nelson,

and Patel) has disclosed the Y-TZP slurry development and materials processing part of this research to the Virginia Tech Intellectual Properties LINK+LICENSE+LAUNCH department (20–112 – Processing Method for Fabrication of Complex Functional Ceramic Parts).

CRediT authorship contribution statement

R. Joey Griffiths: Data curation. Jake K. Yoder: Data curation. Xiaoyu Zheng: Resources, Supervision. Hang Z. Yu: Funding acquisition, Supervision, Writing – review & editing. Hunter A. Rauch: Writing – original draft, Investigation, Formal analysis, Data curation. Huachen Cui: Data curation. Kendall P. Knight: Formal analysis.

Declaration of Competing Interest

The authors declare that they have no known competing financial interests or personal relationships that could have appeared to influence the work reported in this paper.

Acknowledgements

H.Z.Y, H.A.R, K.P.K, R.J.G, and J.K.Y would like to acknowledge their support from the National Science Foundation (CMMI-1853893) as well as the Department of Materials Science and Engineering at Virginia Tech through a senior design project. H.C. and X.Z. thank the Office of Naval Research (N00014-20-1-2504) and Air Force Office of Scientific Research (FA9550-18-1-0299) for funding support. The authors would also like to thank Drew Arvan, Kyle Nelson, and Neal Patel for assistance in slurry synthesis. This work was performed in part at the Nanoscale Characterization and Fabrication Laboratory, which is supported by the Virginia Tech National Center for Earth and Environmental Nanotechnology Infrastructure (NanoEarth), a member of the National Nanotechnology Coordinated Infrastructure (NNCI), supported by NSF (ECCS 1542100 and ECCS 2025151).

Appendix A. Derivation of Eq. (2) in the main text

For photocurable ceramic slurries, the depth of penetration D_P depends on the solid loading fraction V_S and the refractive index difference Δn between the monomer and ceramic [23]:

$$D_P = \frac{2\mathrm{d}\lambda}{3V_S \Delta n^2 h} \tag{A1}$$

Here, d is the ceramic particle size, and λ is the light wavelength. The variable h is the interparticle spacing and can be written as [45]:

$$h = d\left(\left(\frac{\boldsymbol{V}_{Smax}}{\boldsymbol{V}_S}\right)^{1/3} - 1\right) \tag{A2}$$

In this formulation, V_S^{max} is the solid loading fraction at the densest packing possible for a given particle size distribution. For a randomly packed, monodisperse powder like the Y-TZP used in this work, $V_{S_{max}} \approx 0.6$. Combining Eqs. (A1) and (A2) yields Eq. (2):

$$\boldsymbol{D}_{P} = \frac{2\lambda}{3\Delta n^{2} V_{S} \left(\left(\frac{V_{S}^{max}}{V_{S}} \right)^{1/3} - 1 \right)}$$

References

- B.G. Compton, J.A. Lewis, 3D-printing of lightweight cellular composites, Adv. Mater. 26 (2014) 5930–5935. https://doi.org/10.1002/adma.201401804.
- [2] T.A. Schaedler, W.B. Carter, Architected cellular materials, Annu. Rev. Mater. Res. 46 (2016) 187–210, https://doi.org/10.1146/annurev-matsci-070115-031624.
- [3] D. Snelling, Q. Li, N. Meisel, C.B. Williams, R.C. Batra, A.P. Druschitz, Lightweight metal cellular structures fabricated via 3D printing of sand cast molds, Adv. Eng. Mater. 17 (2015) 923–932, https://doi.org/10.1002/adem.201400524.
- [4] D.W. Abueidda, M. Bakir, R.K. Abu Al-Rub, J.S. Bergström, N.A. Sobh, I. Jasiuk, Mechanical properties of 3D printed polymeric cellular materials with triply periodic minimal surface architectures, Mater. Des. 122 (2017) 255–267, https://doi.org/10.1016/j.matdes.2017.03.018.
- [5] A. Mirabolghasemi, A.H. Akbarzadeh, D. Rodrigue, D. Therriault, Thermal conductivity of architected cellular metamaterials, Acta Mater. 174 (2019) 61–80, https://doi.org/10.1016/j.actamat.2019.04.061.
- [6] J. Xue, L. Gao, X. Hu, K. Cao, W. Zhou, W. Wang, Y. Lu, Stereolithographic 3D printing-based hierarchically cellular lattices for high-performance quasi-solid

- supercapacitor, Nano Micro Lett. 11 (2019) 1–13, https://doi.org/10.1007/
- [7] M. Benedetti, A. du Plessis, R.O. Ritchie, M. Dallago, S.M.J. Razavi, F. Berto, Architected cellular materials: a review on their mechanical properties towards fatigue-tolerant design and fabrication, Mater. Sci. Eng. R. Rep. 144 (2021), 100606, https://doi.org/10.1016/j.mser.2021.100606.
- [8] G. Dong, Y. Tang, Y.F. Zhao, A survey of modeling of lattice structures fabricated by additive manufacturing, J. Mech. Des. Trans. (2017), https://doi.org/10.1115/ 1.4037305.
- [9] A. Lai, Z. Du, C.L. Gan, C.A. Schuh, Shape memory and superelastic ceramics at small scales, Science 341 (2013) 1505–1508, https://doi.org/10.1126/ science 1239745
- [10] H.A. Rauch, Y. Chen, K. An, H.Z. Yu, In situ investigation of stress-induced martensitic transformation in granular shape memory ceramic packings, Acta Mater. 168 (2019) 362–375, https://doi.org/10.1016/j.actamat.2019.02.028.
- [11] H.A. Rauch, H.Z. Yu, Effects of mechanical constraint on thermally induced reverse martensitic transformation in granular shape memory ceramic packings, J. Appl. Phys. 128 (2020), https://doi.org/10.1063/5.0035041.
- [12] V.S. Raut, T.S. Glen, H.A. Rauch, H.Z. Yu, S.T. Boles, Stress-induced phase transformation in shape memory ceramic nanoparticles, J. Appl. Phys. 126 (2019), https://doi.org/10.1063/1.5118818.
- [13] X. Zeng, N. Arai, K.T. Faber, Robust cellular shape-memory ceramics via gradient-controlled freeze casting, Adv. Eng. Mater. 21 (2019), 1900398, https://doi.org/10.1002/adem.201900398.
- [14] E.L. Pang, G.B. Olson, C.A. Schuh, Role of grain constraint on the martensitic transformation in ceria-doped zirconia, J. Am. Ceram. Soc. 104 (2021) 1156–1168, https://doi.org/10.1111/jace.17526.
- [15] A.G. Evans, A.H. Heuer, Transformation toughening in ceramics: martensitic transformations in crack tip stress fields, J. Am. Ceram. Soc. 63 (1979) 241–248.
- [16] D. Lyon, J. Chevalier, L. Gremillard, C. a D. Cam, Zirconia as a biomaterial, Compr. Biomater. 20 (2011) 95–108, https://doi.org/10.1016/B978-0-08-055294-1.00017-9.
- [17] J. Chevalier, L. Gremillard, Ceramics for medical applications: a picture for the next 20 years, J. Eur. Ceram. Soc. 29 (2009) 1245–1255, https://doi.org/10.1016/ j.jeurceramsoc.2008.08.025.
- [18] J. Chevalier, L. Gremillard, A.V. Virkar, D.R. Clarke, The tetragonal-monoclinic transformation in zirconia: lessons learned and future trends, J. Am. Ceram. Soc. 92 (2009) 1901–1920, https://doi.org/10.1111/j.1551-2916.2009.03278.x.
- [19] W.D.J. Callister, D.G. Rethwisch, Materials Science and Engineering: An Introduction, 7th ed., John Wiley & Sons, Quebec, 2007.
- [20] S.M. Ueland, C.A. Schuh, Grain boundary and triple junction constraints during martensitic transformation in shape memory alloys, J. Appl. Phys. 114 (2013), https://doi.org/10.1063/1.4817170.
- [21] R. He, W. Liu, Z. Wu, D. An, M. Huang, H. Wu, Q. Jiang, X. Ji, S. Wu, Z. Xie, Fabrication of complex-shaped zirconia ceramic parts via a DLP- stereolithographybased 3D printing method, Ceram. Int. 44 (2018) 3412–3416, https://doi.org/ 10.1016/j.ceramint.2017.11.135.
- [22] M. Shen, W. Qin, B. Xing, W. Zhao, S. Gao, Y. Sun, T. Jiao, Z. Zhao, Mechanical properties of 3D printed ceramic cellular materials with triply periodic minimal surface architectures, J. Eur. Ceram. Soc. 41 (2021) 1481–1489, https://doi.org/10.1016/j.jeurceramsoc.2020.09.062.
- [23] S. Zakeri, M. Vippola, E. Levänen, A comprehensive review of the photopolymerization of ceramic resins used in stereolithography, Addit. Manuf. 35 (2020), 101177, https://doi.org/10.1016/j.addma.2020.101177.
- [24] R.B. Osman, A.J. van der Veen, D. Huiberts, D. Wismeijer, N. Alharbi, 3D-printing zirconia implants; a dream or a reality? An in-vitro study evaluating the dimensional accuracy, surface topography and mechanical properties of printed zirconia implant and discs, J. Mech. Behav. Biomed. Mater. 75 (2017) 521–528, https://doi.org/10.1016/j.jmbbm.2017.08.018.
- [25] M. Borlaf, L. Conti, T. Graule, Influence of tensile edge design and printing parameters on the flexural strength of ZrO2 and ATZ bars prepared by UV-LCM-DLP, Open Ceram. 5 (2021), 100066, https://doi.org/10.1016/j. oceram.2021.100066.
- [26] L. Conti, D. Bienenstein, M. Borlaf, T. Graule, Effects of the layer height and exposure energy on the lateral resolution of zirconia parts printed by lithographybased additive manufacturing, Materials (2020), https://doi.org/10.3390/ mai/3061317
- [27] M. Borlaf, N. Szubra, A. Serra-Capdevila, W.W. Kubiak, T. Graule, Fabrication of ZrO2 and ATZ materials via UV-LCM-DLP additive manufacturing technology, J. Eur. Ceram. Soc. 40 (2020) 1574–1581, https://doi.org/10.1016/j. jeurceramsoc.2019.11.037.
- [28] J. Sun, J. Binner, J. Bai, 3D printing of zirconia via digital light processing: optimization of slurry and debinding process, J. Eur. Ceram. Soc. 40 (2020) 5837–5844, https://doi.org/10.1016/j.jeurceramsoc.2020.05.079.
- [29] J. Sun, X. Chen, J. Wade-Zhu, J. Binner, J. Bai, A comprehensive study of dense zirconia components fabricated by additive manufacturing, Addit. Manuf. 43 (2021), 101994, https://doi.org/10.1016/j.addma.2021.101994.
- [30] D.A. Komissarenko, P.S. Sokolov, A.D. Evstigneeva, I.A. Shmeleva, A.E. Dosovitsky, Rheological and curing behavior of acrylate-based suspensions for the DLP 3D printing of complex zirconia parts, Materials (2018), https://doi.org/10.3390/ mail122350
- [31] J. Ebert, E. Özkol, A. Zeichner, K. Uibel, Ö. Weiss, U. Koops, R. Telle, H. Fischer, Direct inkjet printing of dental prostheses made of zirconia, J. Dent. Res. 88 (2009) 673–676, https://doi.org/10.1177/0022034509339988.

- [32] A. Ghazanfari, W. Li, M.C. Leu, J.L. Watts, G.E. Hilmas, Additive manufacturing and mechanical characterization of high density fully stabilized zirconia, Ceram. Int. 43 (2017) 6082–6088, https://doi.org/10.1016/j.ceramint.2017.01.154.
- [33] H. Shao, D. Zhao, T. Lin, J. He, J. Wu, 3D gel-printing of zirconia ceramic parts, Ceram. Int. 43 (2017) 13938–13942, https://doi.org/10.1016/j. ceramint.2017.07.124.
- [34] K.J. Jang, J.H. Kang, J.G. Fisher, S.W. Park, Effect of the volume fraction of zirconia suspensions on the microstructure and physical properties of products produced by additive manufacturing, Dent. Mater. 35 (2019) e97–e106, https://doi.org/10.1016/j.dental.2019.02.001.
- [35] X.Y. Yap, I. Seetoh, W.L. Goh, P. Ye, Y. Zhao, Z. Du, C.Q. Lai, C.L. Gan, Mechanical properties and failure behaviour of architected alumina microlattices fabricated by stereolithography 3D printing, Int. J. Mech. Sci. 196 (2021), 106285, https://doi. org/10.1016/j.ijmecsci.2021.106285.
- [36] J.W. Halloran, Ceramic stereolithography: additive manufacturing for ceramics by photopolymerization, Annu. Rev. Mater. Res. 46 (2016) 19–40, https://doi.org/ 10.1146/annurev-matsci-070115-031841.
- [37] W. Harrer, M. Schwentenwein, T. Lube, R. Danzer, Fractography of zirconiaspecimens made using additive manufacturing (LCM) technology, J. Eur. Ceram. Soc. 37 (2017) 4331–4338, https://doi.org/10.1016/j.jeurceramsoc.2017.03.018.
- [38] J. Bauer, S. Hengsbach, I. Tesari, R. Schwaiger, O. Kraft, High-strength cellular ceramic composites with 3D microarchitecture, Proc. Natl. Acad. Sci. U. S. A. 111, 2014. 2453–2458. https://doi.org/10.1073/pnas.1315147111.
- [39] Z. Pan, D. Wang, X. Guo, Y. Li, Z. Zhang, C. Xu, High strength and microwaveabsorbing polymer-derived SiCN honeycomb ceramic prepared by 3D printing, J. Eur. Ceram. Soc. 42 (2022) 1322–1331, https://doi.org/10.1016/j. jeurceramsoc.2021.12.003.
- [40] W. Zhao, C. Wang, B. Xing, M. Shen, Z. Zhao, Mechanical properties of zirconia octet truss structures fabricated by DLP 3D printing, Mater. Res. Express 7 (2020), https://doi.org/10.1088/2053-1591/aba643.
- [41] N.A. Fleck, V.S. Deshpande, M.F. Ashby, Micro-architectured materials: Past, present and future, Proc. R. Soc. A Math. Phys. Eng. Sci. 466 (2010) 2495–2516. https://doi.org/10.1098/rspa.2010.0215.
- [42] M. Scheffler, P. Colombo (Eds.), Cellular Ceramics: Structure, Manufacturing, Properties, and Applications, Wiley-VCH, Weinheim, 2005.
- [43] V. Jain, R. Johnson, I. Ganesh, B.P. Saha, Y.R. Mahajan, Effect of rubber encapsulation on the comparative mechanical behaviour of ceramic honeycomb and foam, Mater. Sci. Eng. A. 347 (2003) 109–122, https://doi.org/10.1016/ S0921-5093(02)00587-7.
- [44] H.Z. Yu, M. Hassani-Gangaraj, Z. Du, C.L. Gan, C.A. Schuh, Granular shape memory ceramic packings, Acta Mater. 132 (2017) 455–466, https://doi.org/10.1016/j. actamat.2017.04.057.
- [45] T. Hao, R.E. Riman, Calculation of interparticle spacing in colloidal systems, J. Colloid Interface Sci. 297 (2006) 374–377, https://doi.org/10.1016/j. icis.2004.10.014.
- [46] H. Cui, R. Hensleigh, D. Yao, D. Maurya, P. Kumar, M.G. Kang, S. Priya, X. (Rayne) Zheng, Three-dimensional printing of piezoelectric materials with designed anisotropy and directional response, Nat. Mater. 18 (2019) 234–241, https://doi. org/10.1038/s41563-018-0268-1.
- [47] T. Wierzbicki, Crushing analysis of metal honeycombs, Int. J. Impact Eng. 1 (1983) 157–174, https://doi.org/10.1016/0734-743X(83)90004-0.
- [48] L.J. Gibson, M.F. Ashby, G.S. Shajer, C.I. Robertson, The Mechanics of Two-Dimensional Cellular, Mater., Proc. R. Soc. Lond. Ser. A Math. Phys. Sci. 382 (1982) 25–42
- [49] Zirconia, 2019. www.tosoh.com.
- [50] Materials Property Chart, 2021. (https://www.ceramics.net/sites/default/files/stc-material-brochure-zirconia-ceramic-web-01052021.pdf).
- [51] M.L. Griffith, J.W. Halloran, Freeform fabrication of ceramics via stereolithography, J. Am. Ceram. Soc. 79 (1996) 2601–2608, https://doi.org/ 10.1111/j.1151-2916.1996.tb09022.x.
- [52] M. Borlaf, A. Serra-Capdevila, C. Colominas, T. Graule, Development of UV-curable ZrO2 slurries for additive manufacturing (LCM-DLP) technology, J. Eur. Ceram. Soc. 39 (2019) 3797–3803, https://doi.org/10.1016/j.jeurceramsoc.2019.05.023.
- [53] C.S.C. Inc., Ciba Darocur TPO, (2001) 1–3.
- [54] P. Sehnal, K. Harper, a T. Rose, D.G. Anderson, W.A. Green, B. Husar, M. Griesser, R. Liska, Novel Phosphine Oxide Photoinitiators, Radtech Conf, 2014.
- [55] O. Santoliquido, P. Colombo, A. Ortona, Additive manufacturing of ceramic components by digital light processing: a comparison between the "bottom-up" and the "top-down" approaches, J. Eur. Ceram. Soc. 39 (2019) 2140–2148, https://doi. org/10.1016/j.jeurceramsoc.2019.01.044.
- [56] J. Sun, J. Binner, J. Bai, Effect of surface treatment on the dispersion of nano zirconia particles in non-aqueous suspensions for stereolithography, J. Eur. Ceram. Soc. 39 (2019) 1660–1667, https://doi.org/10.1016/j.jeurceramsoc.2018.10.024.
- [57] P.M. Kelly, L.R.F. Rose, The martensitic transformation in ceramics its role in transformation toughening, Prog. Mater. Sci. 47 (2002) 463–557, https://doi.org/ 10.1016/S0079-6425(00)00005-0.
- [58] E. Moshkelgosha, M. Mamivand, Phase field modeling of crack propagation in shape memory ceramics – application to zirconia, Comput. Mater. Sci. 174 (2020), 109509, https://doi.org/10.1016/j.commatsci.2019.109509.
- [59] F.R. Chien, F.J. Ubic, V. Prakash, A.H. Heuer, Stress-induced martensitic transformation and ferroelastic deformation adjacent microhardness indents in tetragonal zirconia single crystals, Acta Mater. 46 (1998) 2151–2171, https://doi. org/10.1016/S1359-6454(97)00444-8.
- [60] I.R. Crystal, C.A. Schuh, Grain-size effect on cracking accumulation in yttria-doped zirconia ceramics during cyclic martensitic transformations, Acta Mater. 209 (2021), 116789, https://doi.org/10.1016/j.actamat.2021.116789.

- [61] N.E. Dowling, Mechanical Behavior of Materials, fourth ed., Pearson Education Limited, Essex, England, 2013.
- [62] T. Kosmac, C. Oblak, P. Jevnikar, N. Funduk, L. Marion, The effect of surface grinding and sandblasting on flexural strength and reliability of Y-TZP zirconia ceramic T, Dent. Mater. 15 (1999) 426–433, https://doi.org/10.1016/0038-1101 (68)90151-2.
- [63] Z. Du, X.M. Zeng, Q. Liu, C.A. Schuh, C.L. Gan, Superelasticity in micro-scale shape memory ceramic particles, Acta Mater. 123 (2017) 255–263, https://doi.org/ 10.1016/j.actamat.2016.10.047.
- [64] S. Xie, H. Zhou, Analysis and optimisation of parameters influencing the out-ofplane energy absorption of an aluminium honeycomb, Thin Walled Struct. 89 (2015) 169–177, https://doi.org/10.1016/j.tws.2014.12.024.